ADVANCED FUNCTIONAL MATERIALS
www.afm-journal.de

Unraveling Polymer–Ion Interactions in Electrochromic Polymers for their Implementation in Organic Electrochemical Synaptic Devices

Heejung Roh, Shuwen Yue, Hang Hu, Ke Chen, Heather J. Kulik, and Aristide Gumyusenge**

Owing to low-power, fast and highly adaptive operability, as well as scalability, electrochemical random-access memory (ECRAM) technology is one of the most promising approaches for neuromorphic computing based on artificial neural networks. Despite recent advances, practical implementation of ECRAMs remains challenging due to several limitations including high write noise, asymmetric weight updates, and insufficient dynamic ranges. Here, inspired by similarities in structural and functional requirements between electrochromic devices and ECRAMs, high-performance, single-transistor and neuromorphic devices based on electrochromic polymers (ECPs) are demonstrated. To effectively translate electrochromism into electrochemical ion memory in polymers, this study systematically investigates polymer–ion interactions, redox activity, mixed ionic–electronic conduction, and stability of ECPs both experimentally and computationally using select electrolytes. The best-performing ECP-electrolyte combination is then implemented into an ECRAM device to further explore synaptic plasticity behaviors. The resulting ECRAM exhibits high linearity and symmetric conductance modulation, high dynamic range (≈1 mS or ≈6x), and high training accuracy (>84% within five training cycles on a standard image recognition dataset), comparable to existing state-of-the-art ECRAMs. This study offers a promising approach to discover and design novel polymer materials for organic ECRAMs and demonstrates potential applications, taking advantage of mature knowledge basis on electrochromic materials and devices.

1. Introduction

The human brain is considered the most advanced model excelling at simultaneously executing complex tasks such as sensing, reasoning, recognition, control, and movement with minimal power consumption (≈20 W, while computers require >12 times more energy just to recognize a thousand objects).[1–3] A typical fully developed brain consists of a network of over 10^{11} neurons, which transfer information through discrete action potentials or spikes. Biological neurons are interconnected through ≈10^{15} synapses,[4] which serve as storage elements for memory and learning, working in highly parallel, energy-efficient, and fault-tolerant fashion.[5–8] Inspired by this, artificial synapses with co-allocation of memory and computing have been utilized in various memory devices that simulate associative learning.[9–11] Synaptic plasticity is typically emulated in materials with tunable conductance via training processes based on programmed number, timing, frequency, and amplitude of pre- and post-synaptic spikes.

H. Roh, A. Gumyusenge
Massachusetts Institute of Technology
Department of Materials Science & Engineering
77 Massachusetts Ave, Cambridge, MA 02139, USA
E-mail: aristide@mit.edu

S. Yue, H. J. Kulik
Massachusetts Institute of Technology
Department of Chemical Engineering
77 Massachusetts Ave, Cambridge, MA 02139, USA
E-mail: hjkulik@mit.edu

H. Hu, K. Chen
Purdue University
Department of Chemistry
West Lafayette, IN 47907, USA

H. J. Kulik
Massachusetts Institute of Technology
Department of Chemistry
77 Massachusetts Ave, Cambridge, MA 02139, USA

The ORCID identification number(s) for the author(s) of this article can be found under https://doi.org/10.1002/adfm.202304893

DOI: 10.1002/adfm.202304893

During training of artificial synapses, the synaptic weights are updated via material-dependent switching mechanisms:[12] i) filament forming, ii) charge trapping, iii) ion migration, and iv) reversible electrochemical reaction.[13] Memory devices have thus been developed including two-terminal resistive switches (memristors), phase change memory (PCM), resistive random-access memory (ReRAM), magnetic random-access memory (MRAM), and electrochemical random-access memory (ECRAM).[12,14] Despite recent successes in synaptic devices based on such architectures, mostly utilizing inorganic materials, critical challenges persist:[12,14] incompatibility with large-area scalable processing, limitations in terms of processability of phase-pure structures, limited scope of available mobile ionic species, and unsuitability for direct integration with biological matter, limiting potential use in bioelectronics applications. Specifically, asymmetric/nonlinear resistive switching, mostly due to stochastic nature of the conductance tuning (most common during conductive filament formation and rupture) is detrimental to device reliability and learning accuracy.

Among these technologies, ECRAM devices have garnered particular interest owing to their working mechanism based on ionic insertion/extraction (analogous to biological memory), their superior power efficiency, as well as their high-accuracy computing.[15–17] Such ion-based memory has also served as a platform for studying structure-property relationships, enabling researchers to explore learning behaviors in a variety of electrolytic environments. As such, high-speed and high-accuracy electrochemical synthetic synapses utilizing small-size ions (e.g., H^+ and Li^+) have been demonstrated.[18–21] ECRAM-based technologies have also been proposed for seamless integration with biology, given the similarity in the working mechanism, as well as their low and body-safe driving voltages. Particularly, organic-based ECRAMs have been studied as potent tools for bio-abiotic communication such as brain-computer interfaces (BCI), biosensors, and wearable devices, enabling advanced technologies at the interface with biology.[22–26] For instance, high-performance electrochemical neuromorphic organic devices (ENODe) with i) low operating energy (<10 pJ for 10^3 μm^2 devices), ii) distinct conductance states (>500 states) that are non-volatile within input voltage of 1 V, and iii) superior linearity and stability have been demonstrated.[26,27] Melianas et al. have even employed this architecture to demonstrate high dynamic range (≈4x), energy efficient programming (≈1 V, 300 ns pulses) with high durability (>10^9 write-read operations) using poly(2-(3,3-bis(2-(2-(2-methoxyethoxy)ethoxy)ethoxy)-[2,2-bithiophen]−5-yl)thieno[3,2-b]thiophene) (p(g2T-TT)) incorporated into ECRAM architecture as the channel material.[24]

Despite recent successful demonstrations in polymer-based ECRAMs,[24,28,29] several limitations remain before such technologies can be implemented:[11,30–32] 1) Often, the writing and reading processes must be decoupled to learn and ensure stability. This is realized via circuitry turn on and off, physically disconnecting, or employing additional devices such as conductive bridge memory (CBM) between the gate and channel, which complicates circuit design and thus applicational implementation. 2) Unwanted redox reactions (e.g., overoxidation, side reactions) of the channel materials often affect device stability and operability. 3) No single material system has yet to meet the entire set of stringent neuromorphic device metrics (e.g., programming linearity, fast switching, low operating current/voltage, low switching energy, high endurance) thus warranting further materials and device investigation.

In the above-discussed successful demonstrations of organic ECRAMs, organic mixed ionic–electronic conductors (OMIECs) are typically used for their coupled transport. They are attractive for translating signals across interfaces (e.g., semiconductor-electrolyte interfaces) as well as imitating biological functions. OMIECs, commonly conjugated polymers tethered with polar side groups,[33] facilitate the charge coupling owing to their dynamic, open-structured, and ion-compatible nature. As a result, these materials are often used for fast switching and energy-efficient signal transduction, tunable charge retention, wide dynamic range, and high-endurance and reliable learning.[13,23,34] Additionally, OMIECs can be chemically fine-tuned through backbone and side-chain engineering, enabling facile modulation of energy-levels, and thus properties, for specific application. This structural tunability also allows OMIECs to function vis-à-vis a wide range of electrolytes. Since the electrolyte is another key factor determining the effectiveness and behavior of ionic–electronic coupling besides structure, the ability of OMIECs to interface with specific environments guides the usefulness of the resulting devices.

Here, we investigate the use of electrochromic polymers (ECPs), which have often been overlooked in other electronic devices due to their modest electronic transport capabilities, as OMIEC candidates in ECRAM devices. We target to leverage electrochromism as a widely studied property in polymers to investigate polymer-electrolyte interactions and guide the design of organic ECRAMs (Figure **1**a). We use spectro-electrochemical characterizations and theoretical calculations to study the ionic insertion kinetics, redox activity, mixed conduction, and switching stability of ECPs and leverage these properties in memory devices. The best-performing ECP-electrolyte combination is then employed to further explore resulting synaptic plasticity behaviors. We then demonstrate a high-performance and single transistor-based neuromorphic device using the ECP-based ECRAM. The neuromorphic device exhibits highly linear and symmetrical conductance modulation, a dynamic range over 6x, and high training accuracy (>84% over five learning cycles) using a typical image recognition dataset. Through this study, we show the importance of maximizing both ionic insertion and electronic transport, concomitantly, in organic electrochemical memory materials and provide fundamental understanding on polymer–ion interactions. We thus demonstrate that by leveraging the well-established knowledge on electrochromic materials and devices, we can garner new insights for enhancing ECRAM performance and guide next-generation organic memory device designs.

2. Results and Discussion

ECPs are π-conjugated systems that change color upon electrochemical oxidation and/or reduction.[35–37] Such polymers are increasingly becoming common in electrochromic devices (ECDs)[35,37–39] such as smart windows, goggles, sunroofs, and displays; technologies in which reliable and durable coloration switching is crucial (Figure 1b). In addition to low-power color switching, ECPs are also attractive owing to their large-scale synthesizability and compatibility with roll-to-roll coating for large

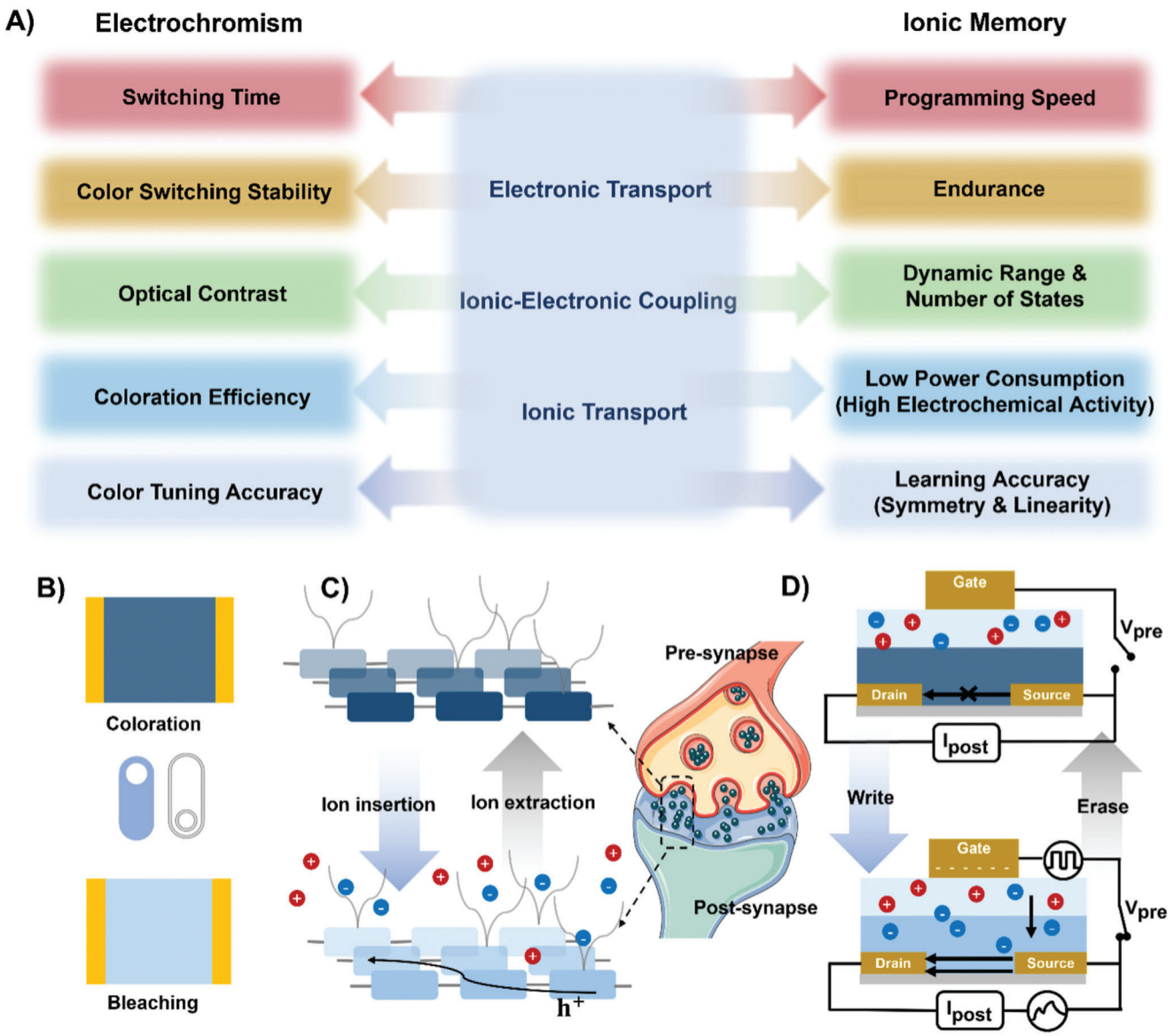

Figure 1. a) Schematic illustration showing relevant performance metrics relating electrochromism and ionic memory via three physical processes; electronic transport, ionic transport, and ionic–electronic coupling. b–d) Comparison between electrochromic devices (ECDs) and artificial synapses (e.g., OECT, ECRAM) where electrochromic polymers (ECPs) are utilized as active materials which change the optoelectronic state upon electrochemical doping.

area devices. For a color change to occur electrochemically, the color-changing polymer functions as a working electrode separated from a secondary electrode by an ion source or electrolyte, in a battery-like manner. Upon application of a small potential (≈1 V) between the two electrodes, the working electrode is either oxidized or reduced, while counter ions are inserted into the electrode for charge compensation. This process alters the light absorption profile in the case of ECPs as illustrated in Figure 1c. Herein, we investigate the same working principle, where instead of coloration, we monitor the change in the conductance state of the polymer as a function of applied bias (Figure 1d). To enable fast and stable switching in ECDs, the color-changing polymer must uptake ions rapidly and must do so reversibly. Additionally, the polymer must sustain many switching events to yield long-term function of the windows or displays.

Though the above-listed material properties are also desired in electrochemical neuromorphic devices, ECPs have been largely overlooked for potential use in other electronic devices due to low charge charrier mobilities.[41] In electrochemical memory devices, where both charge capacitance and electronic mobility are crucial, we hypothesized that unraveling charge insertion and retention in ECPs, widely studied for opto-electrical responsiveness, would enable future design/discovery of high-performance materials for memory. By translating the coloration states into programmable conductance states, we were intrigued by whether polymer electrochromism can be leveraged in memory devices.

That is, analogous to color change (i.e., change in absorption profile in the visible range), we probed conductance modulation (resistive switching) for memory devices. We aimed to correlate fundamental processes (electronic transport, ionic transport, and ionic–electronic coupling) to resulting performance metrics in terms of opto-electronic response of polymer to external stimuli (Figure 1a; Figure S1, Supporting Information). Though the current work focuses on linking coloration control to ionic memory, other similarities in these systems can be drawn and have been detailed in previous literatures.[41] To effectively employ ECPs for ionic memory, both the fundamental similarities and differences between the two device architectures were investigated. Although the two systems share electrochemical working principles, stricter electrical conduction requirements must be met in synaptic devices. Here, we focused on structural tuning, polymer-electrolyte compatibility, and charge transport in ECPs to guide performance optimization in ECRAMs.

Extensive studies on the electrochromic properties of polymers (e.g., hue, coloration time, color contrast, and color efficiency)[42–44] have been conducted through systematic exploration of their molecular structures. Typically, copolymerization of various repeat units in appropriate ratios is used to tune energy levels and polymer-electrolyte interactions.[37,44–48] Though such strategies have matured in ECDs, they have rarely been utilized in optimizing synaptic transistors. Among the most studied ECPs, poly(3,4-(alkylenedioxy)thiophene)s (PxDOTs), especially polymers based on 3,4-propylenedioxythiophene (ProDOT)[49,50] have been intensively utilized owing to their properties such as i) high charge storage capacity, ii) low-energy requirement for redox switching, and iii) high cycling stability.[51] In ProDOT derivatives, these properties have been rationalized both kinetically and thermodynamically. The substitution of the ethylene bridge with propylene, offering a larger ring, results in a more twisted backbone and microstructurally open morphology of the corresponding polymer, which is favorable for incorporating large amounts of ions within relevant time scale as well as fast diffusion. Lengthening and branching the solubilizing side chains on ProDOT (from dibutyl to dihexyl-and bis(2-ethylhexyl)-substituted) have shown to further improve such ion kinetics and thus the switching time.[42–44] Thermodynamically, the disubstitution of π-donating oxygen atoms lowered HOMO (highest occupied molecular orbital) levels (≈0.1–0.3 eV) relative to the air oxidation threshold (5.2–5.3 eV vs vacuum),[35] rendering the resulting polymers facile to oxidize upon biasing. Facile oxidation enables device operation at a lower voltage and is also favorable for redox reversibility given the narrow electrochemical window of aqueous-based electrolytes. Such redox stability (i.e., reversible redox reaction) is further ensured by the alkylene bridge shielding the conjugated backbone from undesired irreversible side reactions such as nucleophilic attack.

Albeit its high electrochromic capabilities (e.g., color contrast) based on high ion-compatibility and redox stability,[52] the homopolymer of ProDOT is known to exhibit slow optical transition (~seconds)[51] due to the lack of backbone planarity. Meanwhile, a donor–acceptor (D–A) copolymerization strategy has been utilized for tailoring optoelectronic properties; it is mainly employed for achieving mid-visible range colors in electrochromic polymers by leveraging intrinsically distinct dual optical transitions.[53] Besides facile tuning of energy levels, the D–A approach enables adjustment of backbone rigidity/planarity and thus microstructure, as well as achieving narrow band gaps between 1.6 and 1.8 eV through a push-pull effect.[54] Such an effect results in extended conjugation with a more delocalized electron cloud, which is beneficial for enhancing electronic conductivity which is desired in OMIECs. Hence, the abovementioned drawbacks can be overcome by copolymerizing ProDOT with other complementary moieties.

Meanwhile, it is widely accepted that including heterocyclic compounds with a nitrogen atom arranged in a pyridine-like structure into a more electron-rich system can efficiently lower LUMO (lowest unoccupied molecular orbital) levels and thus decrease the energy band gaps of D–A π-conjugated polymers upon hybridization.[55–57] For instance, benzothiadiazole (BTD) has been used for such energy tuning in addition to inducing backbone rigidity/planarity, leading to enhanced coherence length of the conjugated backbone and thus electrical percolation. However, though this strategy enhances charge carrier mobility, it comes at the expense of high oxidation potential, limited solubility, and irreversible redox reaction, especially in water, due to nucleophilic attack at radical cation sites, resulting in the cleavage of oligo(ether) chains and thus degradation of the polymer.[58] Nonetheless, balancing ion compatibility and electronic delocalization via copolymerizing ProDOT and BTD in alternating manner (D-A) has shown to enable electrochromes combining solution processability, high contrast ratios attainable in sub-second switching times, and long-term redox stability.[54] Specifically, electrochromes consisting of three different feed ratios of D(ProDOT)/A(BTD) = 100%, 82.5%, 50% have shown to exhibit optical contrast as well as a memory effect,[59] i.e., retention of colored/bleached state under V_{OFF}, and are thus used here as the model structures. Herein, we employ these three copolymers (**Figure 2**a,e,i) named ECP-100, ECP-82.5, and ECP-50, exhibiting a magenta, black, and blue color in their neutral state, respectively. From solid-state characterizations, UV–vis spectra of the three ECPs are shown in Figure S2 (Supporting Information), and AFM height profiles demonstrating that corresponding spin-coated thin films are homogeneous and uniform (with measured roughness less than ≈3.6 nm) are shown in Figure S3, Supporting Information.

To compare the redox activity of the three ECPs, spectroelectrochemical measurements are carried out in both aqueous (0.1 M $LiPF_6$) and non-aqueous (1-ethyl-3-methylimidazolium bis(trifluoromethyl sulfonylimide) (EMIMTFSI)) electrolytes using a three-electrode cell setup. The spectroscopic (UV–vis) spectra are monitored as a function of the applied electrochemical potential from a reference electrode. As the working potential increases, the intensities of the absorbance peaks corresponding to the π--π^* transition ($\lambda_{max\ (\pi-\pi*)}$ of 646 nm for ECP-100, 544 nm for ECP-82.5, and 623 nm for ECP-50) significantly decreases and completely vanishes above their critical voltages, Figure 2b,f,j and Figure 2c,g,k. Meanwhile, the intensity of the absorption peak in the near-infrared (NIR) region ($\lambda_{polaron}$ ≈1150 nm) increases, indicating higher charge carrier density and thus conductance due to the generation of radical cation/polaron. This electrochemical switching corresponds to a transition from colored (neutral) to transmissive/bleached (doped) states. ECP-50 showed a dramatic decrease in $\lambda_{max\ (\pi-\pi*)}$ at ≈+0.2 V (vs Ag/Ag^+, H_2O), while ECP-82.5 and ECP-100 required a higher voltage budget

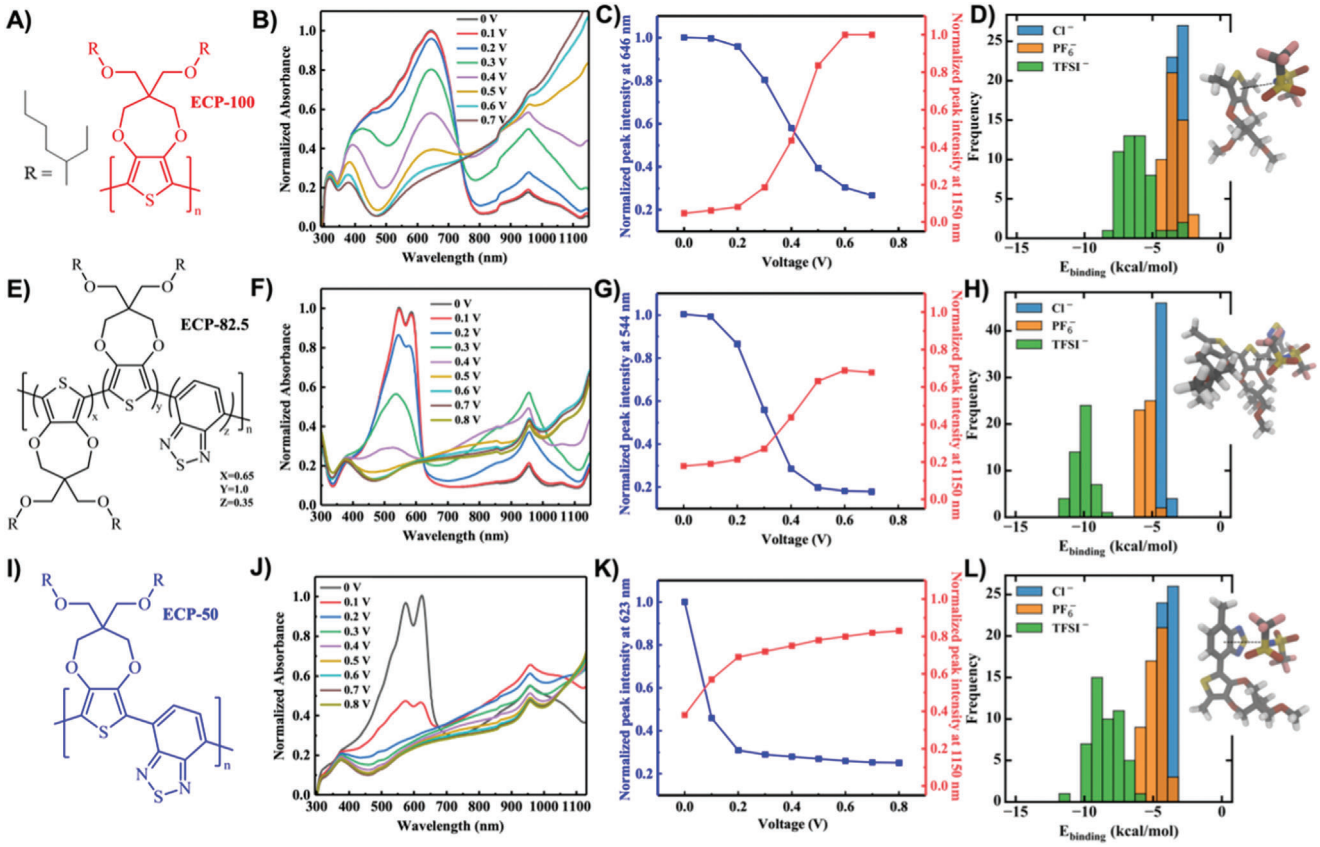

Figure 2. Electrochemical activity of three studied ECPs. Chemical structure of three ECPs with varying ratios of two building units, named a) ECP-100, e) ECP-82.5, and i) ECP-50. Spectro-electrochemical behaviors in 0.1 M $LiPF_6$ of b,c) ECP-100, f,g) ECP-82.5, and j,k) ECP-50. Calculated distributions of binding energies of anions to a single monomer unit of d) ECP-100, h) ECP-82.5, and l) ECP-50, respectively, along with molecular diagrams of the lowest energy configuration of each monomer unit with a $TFSI^-$ anion (the strongest binding anion) where the preferred binding location is orthogonal to the polymer ring plane. C atoms are shown in gray, O atoms in red, H atoms in white, N atoms in blue, S atoms in yellow, and F atoms in pink.

for the collapse of the $\lambda_{max\,(\pi-\pi^*)}$ peak at ≈+0.7 V (vs Ag/Ag^+, H_2O) and ≈+0.6 V (vs Ag/Ag^+, H_2O), respectively. A similar order was observed in non-aqueous electrolytes in which voltages of ≈+0.3 V (vs Ag/Ag^+, neat EMIMTFSI), 0.6 V (vs Ag/Ag^+, neat EMIMTFSI), and 0.6 V (vs Ag/Ag^+, neat EMIMTFSI) were required for ECP-50, ECP-82.5, and ECP-100, respectively (Figure S4, Supporting Information). Such a decrease in intensity at $\lambda_{max\,(\pi-\pi^*)}$ is often accompanied by an increase at $\lambda_{polaron}$ as shown in Figure 2d,h,l and Figure S4 (Supporting Information). As indicated by electrochemical responses, ECP-50 required the lowest voltage for complete electrochemical switching in both aqueous and non-aqueous electrolytes, showing superior dual-redox activity.

To probe the impact of electrolyte choice on the observed electrochemical responses of the three ECPs, the theoretical binding energy quantifying the degree of interaction of three ECPs with three widely utilized anions (Cl^-, PF_6^-, and $TFSI^-$) in water were calculated. All calculations were carried out using density functional theory (DFT) using Orca 5.0.0[60,61] with the B3LYP[62] global hybrid functional along with the empirical D4 dispersion correction,[63] Becke–Johnson basis set damping,[64] and a dev2-TZVP basis set.[65] To better reflect in-operando settings (e.g., solvation effect), the calculations were performed in implicit solvent using the Conductor-like Polarizable Continuum Model (CPCM)[66] with the dielectric constant of bulk water, 78. Each polymer species was represented by a single monomer unit with endpoints capped with CH_3 and with R- groups represented by CH_3 for simplicity. The resultant polymer structure was first geometry-optimized. Then, a single anion was placed with random rotation and random translation near the optimized monomer unit with a minimum distance of 2 Å and a maximum distance of 10–14 Å (depending on the anion and monomer sizes) between all anion-polymer pairs. A constrained optimization was then performed with the monomer unit fixed while the anion was allowed to move to find a low energy positioning of the anion. The anion placement procedure was then repeated 50 times to obtain an ensemble of 50 single anion-polymer binding configurations. A distribution of anion-polymer binding energies (Figure 2d,h,l) was obtained from this ensemble, where the binding energy is defined as: $E_{binding} = E_{polymer/anion} - E_{anion} - E_{polymer}$.

Across all three ECP structures, $TFSI^-$, which is the largest in size and thus has the least charge density, showed the highest binding energy followed by PF_6^- and Cl^-, (Figure 2d,h,l). The energetically favored ion configuration with respect to three units indicates that energy becomes lower (i.e., more favorable) when the anion is directly face-on with respect to the seven-membered

ring (insets of Figure 2d,h,l; Figure S5, Supporting Information). In contrast, the binding energy becomes higher (i.e., less favorable) when the anion binds closer to the alkyl chains of the polymer. The results of these calculations are consistent with previous reports which showed that the kinetics of the doping process in redox active polymers is size dependent and optimal for bulkier anions, such as PF_6^- and $TFSI^-$ than smaller atomic anions, like F^- and Cl^-.[46,67] This behavior has been hypothesized to be caused by the hydration shell which is denser for smaller ions, resulting in a lower effective charge density. The shell formation thus shields the interaction between polymer and anion thereby hindering the coupling between radical cation on the polymer and counter-anion (i.e., charge compensation of doped state), leading to higher activation energies for carrier generation.[46,67] Such preferential binding of anions in the order of $Cl^- < PF_6^- < TFSI^-$ also agreed with the spectro-electrochemical results discussed above (Figure S6, Supporting Information). Meanwhile, there was no clear difference in calculated binding energy with varied cations as shown in Figure S7 (Supporting Information), which agrees with previous reports[45,66] and shown experimentally in the following discussion.

Guided by the electrochemical responses of the three ECPs and the calculation results, we then sought to understand how different polymer–ion interactions in ECPs would translate into mixed ionic–electronic conduction and ionic memory. Here we opted to employ an organic electrochemical transistor (OECT) device as a model architecture to, not only investigate mixed ionic–electronic transport characteristics, but also link electrochemical response to synaptic behaviors. In an OECT, upon application of a gate bias through the electrolyte, an ion-mediated bulk (de) doping of a channel material modulates the current flow between the source and drain electrodes.[68–70] The OECT device thus serves not only as a suitable device architecture for ECRAM, but also as a testbed to determine a material's capacity for mixed ionic–electronic conduction. The mixed ionic–electronic conduction capability of organic conductors is typically extracted in terms of transconductance (g_m), which is the ratio of change in drain current output (I_{DS}) in response to the applied gate bias (V_G, above a material dependent threshold, V_{TH}), or its dimension-normalized version is μC^*, which encompasses capacitance and charge carrier mobility.

Figure 3a–c shows representative transfer curves (insets are the extracted transconductance, g_m) from OECT devices based on the ECPs in both aqueous (LiCl and $LiPF_6$) and non-aqueous (EMIMTFSI) electrolytes. Full data of transfer and output curves of three ECPs in diverse electrolytes are shown in Figures S8–10 (Supporting Information). The current response of the OECTs indicates that the ECPs are p-type and operate in accumulation mode (off at $V_G = 0$ V).[69–71] ECP-50 showed to outperform ECP-82.5 and ECP-100 by two orders of magnitude in terms of the channel current in both aqueous and non-aqueous electrolytes. Two representative parameters, V_{TH} and μC*, were extracted from the current response in various electrolytes and are plotted in Figure 3d–f. Regardless of the electrolyte, V_{TH} was found to be the lowest (<≈0.2 V) for the devices based on ECP-50 and increased as the ProDOT ratio increased, with ECP-100 showing the highest value. We interpreted V_{TH} as the ease of ionic species to penetrate and dope the polymer film and turn "on" the OECT channel. The threshold voltage values were thus in agreement with the above discussed electrochemical responses of the three ECP films.

Analogous to the faster bleaching behavior observed in ECP-50 films, the resulting OECT devices showed switch "on" at lower potentials compared to ECP-82.5 and ECP-100. Additionally, regardless of the electrolyte, μC^* was found to be the highest for ECP-50 based devices (Figure 3d–f) with the same device dimensions (L = 50 μm, W = 4.5 mm), showing the value of 97.1 F cm^{-1} V^{-1} $s^{-1,}$ while 0.27 and 0.44 F cm^{-1} V^{-1} s^{-1} were measured for ECP-82.5 and ECP-100, respectively. These results indicate that by tuning the D–A character of the ECPs, both the capacitance and charge mobility are also tuned. We could also deduce that with the ProDOT-BTD copolymerization, a balance between the two units must be investigated to optimize both ionic insertion and electronic transport. The volumetric capacitance quantifies the bulk ionic uptake and storage capability upon doping, which can be calculated by integrating the current response of during cyclic voltammetry (CV). Meanwhile, mobility (μ) quantifies the electronic conductivity in the doped polymer. C^* and μ are often in a trade-off relationship as the former is favored in amorphous (disordered) morphology for facile ion injection, while the latter is optimal in highly crystalline (ordered) morphology for facile intra- and inter-chain ($\pi-\pi$ stacking) electrical charge transport. C^* for each polymer was obtained from the integration of the corresponding voltammogram.[72]

As shown in Figure 3g,h, ECP-100 and ECP-82.5 exhibited a higher C^* of 421.5 and 338.9 F cm^{-3}, respectively, compared to ECP-50 which had a C^* of 301.3 F cm^{-3}. However, the μ_{OECT} trend followed that of μC^*, with ECP-50 >> ECP-82.5, ECP-100, where the respective values were extracted to be 0.32, 0.0008, and 0.001 cm^2 V^{-1} s^{-1}. It is thus important to note that when designing channel materials for ECRAMs, both the capacitance and mobility must be concomitantly optimized. Full CVs of three ECPs in representative aqueous and non-aqueous electrolytes are shown in Figure S11 (Supporting Information). Using ECP-50, the effect of anion size on OECT performance was also investigated to reveal the following order: LiCl, $LiPF_6$, LiTFSI in terms of transconductance and μC^* (Figure S12, Supporting Information), which is in great agreement with the DFT calculation results discussed above. Corresponding voltammograms of ECP-50 in diverse aqueous and non-aqueous electrolytes are also shown in Figure S13 (Supporting Information) and device parameters are summarized in Table S1 (Supporting Information).

Besides coupled ionic–electronic transport, device endurance is another crucial parameter which remains challenging to attain in organic ECRAMs. We thus tested the cycling stability of the three ECPs in both aqueous and non-aqueous environments. Figure 3g,h shows the cyclic voltammograms obtained during the 10th and 500th cycles of the ECP films, and Figure 3i shows the corresponding amount of charge measured during cycling. Notably, ECP-50 showed to retain its capacitance, over 90% of the initial value, in $LiPF_6$ (Figure 3i) compared to <60% in other electrolytes such as LiTFSI (Figure S13, Supporting Information) after 500 cycles. The performance was barely affected by the cation (Na^+ vs Li^+) across ECPs as shown in Figure 3d–f, which is consistent with the calculated binding energy with varied cations in Figure S7 (Supporting Information). This behavior also agrees with previous studies that show p-type OMIECs are activated based on holes generated through electrostatic stabilization

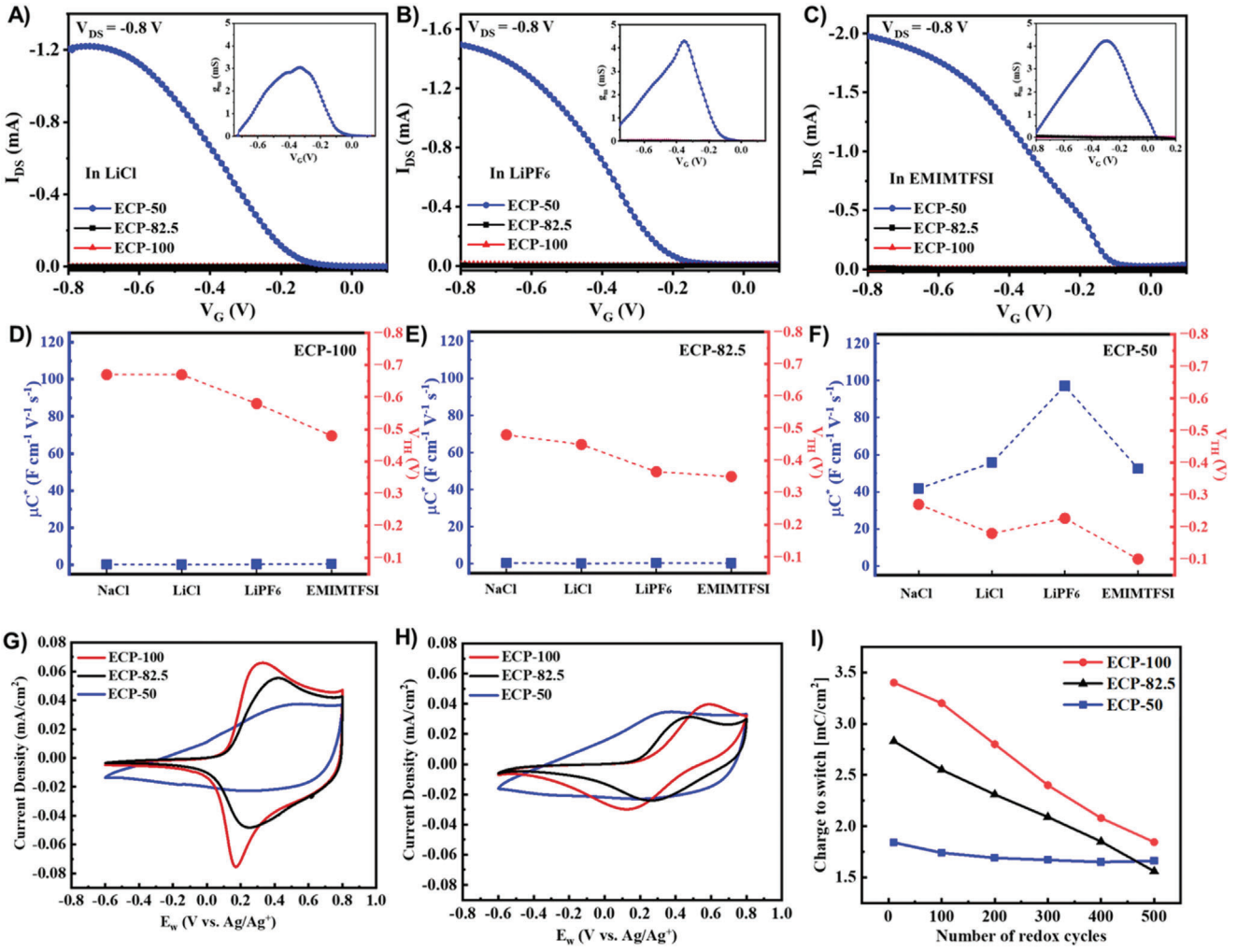

Figure 3. Mixed electronic–ionic conduction property and stability comparison of three ECPs in aqueous and non-aqueous electrolytes. a–c) Transfer curves and transconductance curve (inset) of three ECPs in 0.1 M aqueous solution of a) LiCl, b) $LiPF_6$, and c) neat EMIMTFSI, respectively. d–f) Extracted parameters of three ECPs in various electrolytes. g,h) Cyclic voltammograms of three ECPs in 0.1 M $LiPF_6$, 10th and 500th cycle, respectively. I) Comparison of charge retention capability of three ECPs in 0.1 M $LiPF_6$.

(coupling) with the counterion and are thus mostly affected by the anion rather than the cation. To conclude the comparison of the three ECPs, 500 cycles of CV in various electrolytes were performed to simulate repeated (de) doping during device operation. Figure 3g,h shows the CVs of three ECPs at 10th and 500th cycle in $LiPF_6$, respectively. The cumulative charge with varying redox cycles is shown in Figure 3i. ECP-50 showed the lowest initial capacitance but demonstrated superior stability, maintaining most of the capacity (>90%) over 500 cycles, while ECP-82.5 and ECP-100 were only able to maintain 54% and 55%, respectively. This indicates that the electroactivity of ECP-50 is not compromised and that this material is a robust platform for aqueous andnon-aqueous based electrochemical and bioelectronic devices.

Owing to their minimal voltage requirement for polaron generation, superior electrochemical activity, as well as redox stability, ECP-50 and 0.1 M $LiPF_6$ were selected as the optimal combination for further implementation in ECRAM to probe ion-based synaptic plasticity and memory performance. Ion insertion-based memory devices hold promise not only for enabling co-allocation of memory and processing units, which has been a bottleneck in conventional Von Neumann architecture, but also for high-fidelity artificial neural networks (ANNs) and adaptability.[18] In these devices, electrical pulses sent from a gate electrode that mimics a pre-synaptic neuron are used to tune the injection and extraction of ions from the electrolyte to the semiconducting channel. The change in channel conductance, which is comparable to the post-synaptic current, is recorded as the current flowing between the source and drain contacts.

To investigate the synaptic behaviors of ECP-based devices, for instance, plasticity dependence on spike amplitude (SADP, **Figure 4**a), spike number (SNDP, Figure 4b), and spike frequency (Figure S15, Supporting Information), ECP thin films and 0.1 M $LiPF_6$ aqueous solution were implemented into ECRAM devices and characterized under ambient conditions. Notably, for SADP, the post-synaptic current was recorded upon spiking the gate voltage with pulses (10 ms in width) from 0 V to −0.8 V in a stepwise (0.1 V steps) manner. For SNDP, a range of numbers (from 10 to 300) of gate pulses (−0.6 V with a width

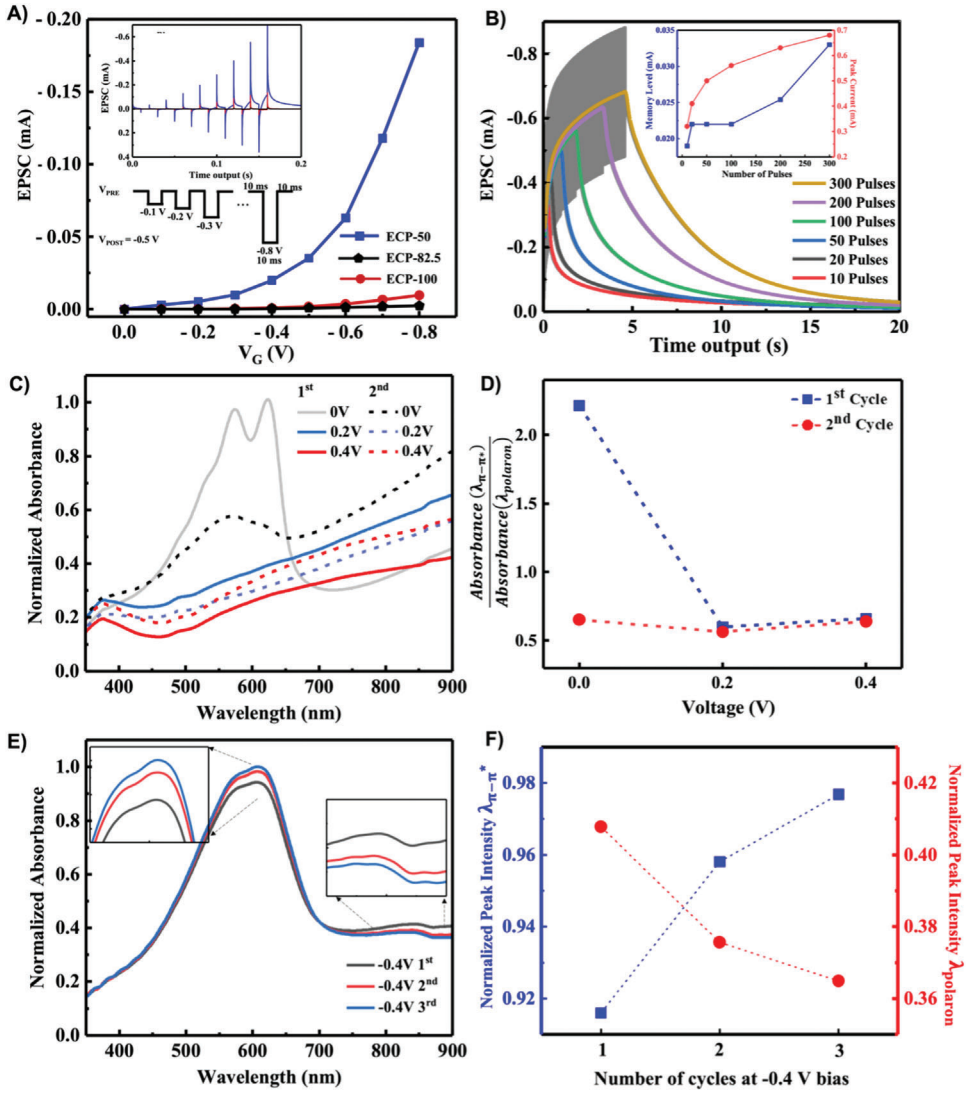

Figure 4. Ion-controlled synaptic behavior of ECPs. a) Spike-amplitude-dependent plasticity (SADP) of transistors based on three ECP films as active channel. b) Spike-number-dependent plasticity (SNDP) of transistors based on ECP-50. (Inset shows the memory level as the excitatory post-synaptic current (EPSC) after holding the channel for 15 s at 0 V and peak current with varying pulse numbers, on Y1 and Y2 axis, respectively). c–f) Memory behavior of ECP-50 probed via spectro-electrochemistry in 0.1 M $LiPF_6$. c) 1st cycle (solid lines) and 2nd cycle (dotted lines) of voltage sweeps. d) Ratio of absorbance at $\lambda_{\pi-\pi*}$ versus $\lambda_{polaron}$. e) Three cycles of spectro-electrochemical measurements under identical bias of opposite polarity (−0.4 V). f) Extracted absorbance at $\lambda_{\pi-\pi*}$ versus $\lambda_{polaron}$.

of 10 ms) were employed while −0.5 V was applied between source and drain. In all synaptic devices, ECP-50 exhibited a significant enhancement in the excitatory post-synaptic current (EPSC) response compared to ECP-82.5 and ECP-100 with two orders of magnitude gap (Figure S14, Supporting Information). ECP-50 was then used for further demonstrations of learning behaviors. The pulse-number-dependent peak current and memory level were extracted as shown in Figure 4b revealing the memristive behavior of the ECP-based device channel. Figure S15 (Supporting Information) also shows the dependence of the post-synaptic current on the spiking frequency in synaptic transistors based on ECP-50. This behavior, particularly the potentiation behavior at higher spike frequency (here, above 20 Hz) and depression a low spiking frequency (here, below 20 Hz), is of great significance for deploying synaptic transistors in tasks which require spike-timing-dependent plasticity.[73]

To further investigate these memristive properties found in ECP-50, we used spectro-electrochemistry and recorded the absorption spectra under two consecutive stepwise voltage sweeping cycles. Figure 4c,d shows that ECP-50 can retain a low value of absorbance ratio between $\lambda_{\pi-\pi*}$ and $\lambda_{polaron}$ throughout second cycle, indicating the retention of generated charge carriers (polarons) and thus the presence of a memory effect. The phenomenon was not observed in both ECP-82.5 and ECP-100. In the latter cases, the spectra of the second cycle of voltage sweeps were nearly identical to those of the first cycle, indicating that the generated polarons cannot be retained without sustained voltage

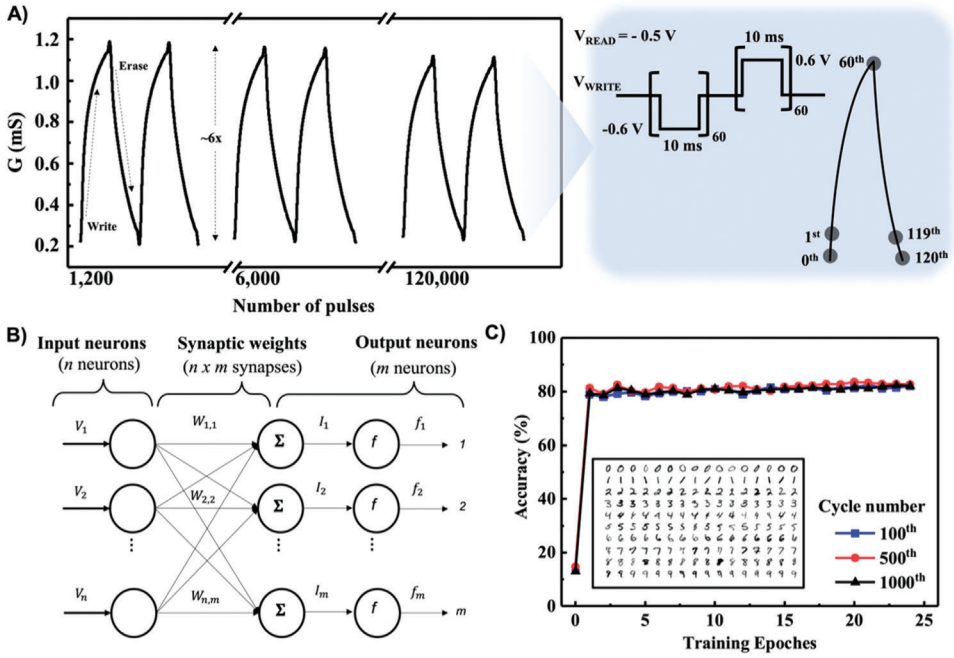

Figure 5. Learning endurance performance and image recognition demonstration of ECP-50. a) Reversible conductance (G) changes of ECP-50 in response to series of train pulses with different polarity (i.e., write/erase), showing excellent endurance. b) Working mechanism of single layer logistic regression model used to recognize standard data set of MINIST[72] (inset in (c)), which is a widely used image dataset for benchmarking machine learning algorithms. c) Accuracy of image recognition tests with respect to training epochs. 100th, 500th, and 1000th cycles were used to further evaluate accuracy retention capability.

(Figure S16, Supporting Information). Additionally, Figure 4e,f demonstrate the reversibility of conductance modulation by being able to recover the initial state (i.e., the reappearance of the prominent π–π^* absorption peak along with decay of the polaron peak) upon bias with opposite polarity (−0.4 V). The level of recovery, which is characterized by a decrease in peak intensity of λ_{polaron} and increase in that of $\lambda_{\pi-\pi*}$, is dependent on the number of biasing cycles.

Given the proven potential of ECP-50 for efficient electrochemical modulation and retention, we further characterized its synaptic plasticity behaviors, which are analogous to the learning and remembering mechanisms in biological neurons, in aqueous electrolyte $LiPF_6$ **Figure 5**a. The reversible conductance changes of ECP-50 in response to a series of pulses with different polarity (i.e., write/erase) demonstrate excellent endurance, which is essential for practical implementation of reliable and high accuracy artificial synapses to perform complex tasks such as image recognition. The same measurements were carried out in non-aqueous electrolyte (EMIMTFSI) as shown in Figure S17 (Supporting Information). The superiority of ECP-50 was demonstrated in both electrolyte environments, with not only linearity and symmetry enabling the same number of potentiation and depression pulses, but also a large dynamic range indicative of an efficient modulation possessing a distinct gap between the high-resistance state and the low-resistance state, as high as ≈1 mS in $LiPF_6$ and ≈0.5 mS in EMIMTFSI. These are two of the most critical yet challenging parameters to achieve simultaneously in a single transistor architecture without an access device or additional step, especially when operating in real-world settings (room temperature and open air).

We then demonstrated object recognition performance of hardware neural networks using the conductance data of 120 representative weight states (100th cycle) of our device. We used 60 potentiation and 60 depression identical training pulses with opposite polarity (inset, Figure 5a). Parameter fitting of the device potentiation and depression for 120 representative weight states is shown in Figure S17 (Supporting Information). MINIST dataset (inset, Figure 5c) which is widely used for benchmarking machine learning algorithms and layer logistic regression model (Figure 5b) was implemented. In each epoch of simulation, the synaptic conductance weights were updated by the training on 60 000 images of handwritten digits. Then, we tested the network using 10 000 testing images and recorded the recognition rates. Recognition rates of 84.3% in 0.1 M $LiPF_6$ aqueous electrolyte and 84.8% in non-aqueous electrolyte EMIMTFSI (Figure S18, Supporting Information) were achieved by single-layer perception within 25 epochs. The ECP-based synaptic device thus demonstrate excellent learning efficiency of the hardware-based backpropagation (HDBP) algorithm,[73–75] which is widely used for optimizing these synaptic weights in the training phase. Such accuracy was also retained throughout 1000 cycles (corresponding to 120 000 pulses) indicating superior endurance and robustness (Figure 5c). Prior to further structural optimization and/or device optimization, the conductance modulation in addition to the training accuracy we demonstrate, simply by optimizing the polymer-electrolyte interactions is of interest for designing novel organic ECRAMs. The dynamic range, switching linearity, and cycling endurance demonstrated using ECP-50 are to par with commonly studied organic mixed conductors, as well as other emerging ECRAM materials (e.g., carbon nanotubes and

MXenes).[73,77] We envision the current computation-guided discussion on polymer–ion interactions to complement emerging chemistry-guided investigations,[13,33,76] toward high performing organic electrochemical memory materials and devices.

3. Conclusion

To the best of our knowledge, this is the first systematic exploration of ECPs for high-performing artificial synapse (i.e., ionic memory), disentangling contributions from key factors including i) structure (e.g., D–A ratio), ii) electrolyte (e.g., solvent, and counter ion), and iii) external input (e.g., V_G). Specifically, the ratio of BTD and ProDOT, two of the well-known building blocks for constructing ECPs for high-performing ECDs, was proven to significantly affect the performance of mixed conduction and ionic memory. In both aqueous and non-aqueous electrolytes, the balanced ratio (D(ProDOT)/A(BTD) = 50%) showed the most well-adjusted μ and C^*, leading to the highest mixed conduction (μC^*), as well as stability, showing potential as a superior dual-redox operable device. The performance of the ECP-based ECRAM we demonstrate is comparable to that of existing state-of-the-art ECRAMs based on a single-transistor architecture without excess device components or additional steps. In future studies, performance can be further improved with device engineering (e.g., scaling down), architectural innovation, and/or encapsulation. This work paves the way for design guidelines based on mature libraries of building blocks of ECPs toward artificial synapse, as well as other applications that are based on the mixed ionic–electronic conduction of organic semiconductors.

4. Experimental Section

Materials: Three ECPs were synthesized following previous reports.[58] Films for characterizations were obtained by spin coating polymer solutions in chloroform followed by annealing (120 °C, 30 min) under vacuum to fully evaporate the solvent. The electrolytes/salts ($LiPF_6$, EMIMTFSI, LiTFSI, LiCl, NaCl) were purchased from Sigma Aldrich.

Device Fabrication for OECTs and ECRAMs: Devices were fabricated by spin coating (900 rpm, 30 s) polymer solutions onto pre-patterned ITO substrates ($L = 50$ µm, $W = 5$ mm) that were purchased from Oscilla and cleaned in the solvents in order of deionized water, acetone, and isopropyl alcohol for 20 min each. Subsequently, the films were annealed at 120 °C for 30 min inside an N_2-filled glovebox and allowed to cool to ambient before electrical measurements under corresponding electrolyte environment.

Electrochemical Characterization: CV measurements were carried out using a conventional three-electrode setup with 4.5 mm wide electrochemical cell to contain the liquid electrolytes during the measurements. Polymer films coated onto ITO serve as a working electrode and a spiral Pt wire was used as a counter electrode, versus an Ag/Ag^+ reference electrode. The volumetric capacitance (C^*) for each polymer was obtained using the obtained CV curves[76] across voltage range of −0.6 to 0.8 V at scan rate of 20 mV s^{-1}, and a 4.5 mm wide electrochemical cell was used to contain the liquid electrolytes during the measurements. The spectroelectrochemical absorption responses were then collected using a Perkin Elmer 1050 UV–vis–NIR spectrophotometer in combination with SP-300 Potentiostat (Biologic), using cuvette to incorporate three-electrode setup that was purchased from Sterna Cell.

Morphological Studies: AFM images were taken using a Bruker Dimension Icon XR SPM under tapping mode with TESPA-V2 tip purchased from Bruker and processed with Gwyddion Software.

Electrical Measurements: Electrical characterizations and pulsed measurements (synaptic device performance) were carried out using a probe station, Keithley 4200 analyzer, in an ambient condition (room temperature and in air). The pulsed measurements were programmed using an ultrafast pulse measure unit coupled with a remote pre-amplified module. OECT performances were obtained by applying a gate voltage from 0 to −0.8 V and the source-drain voltage was set to −0.5 V (unless otherwise indicated). A constant voltage bias (−0.5 V) was applied to either source or drain while the other one is grounded to read the synaptic current flowing between source and drain terminals. To program pulses, voltage pulses ($V_G = 0$ to −0.8 V with both time interval (T_d) and pulse width (Δt) being 10 ms) were applied from gate terminal. For endurance test, a series of identical potentiation pulses were applied with varying numbers (e.g., 10 to 300 times) followed by the application of the same number of depression pulses.

Calculational Details: All calculations were carried out using Orca 5.0.0 with the def2-TZVP basis set, B3LYP global hybrid functional, and the empirical D4 dispersion correction with Becke–Johnson damping. The calculations were performed in implicit solvent using the Conductor-like Polarizable Continuum Model (CPCM) with the dielectric constant of bulk water (78).

Simulation for MNIST Handwritten Digit Recognition: A single-layer perception was simulated using the synaptic devices. This hardware neural network was trained and tested using MINIST, which was a widely used image dataset for benchmarking machine learning algorithms. MINIST comprises of 28 × 28 pixel grayscale images of 70 000 examples from ten digits. Based on this object recognition task, the perceptron was constructed with 785 input neurons, corresponding to the number of image pixels (28 × 28 + 1), and ten output neurons with a softmax layer, corresponding to ten digits. Input and output neurons were fully connected by 7850 (785 × 10) synapses. In the training phase of the hardware neural network, the weights of synapses were updated by comparing the softmax result vectors with digit ground-truth classifications using a cross entropy criterion and Adam optimization algorithm. To optimize these synaptic weights in the training phase, a widely used hardware-based backpropagation (HDBP) algorithm was adopted. More specifically, a differential pair of artificial synapses were used to represent one synaptic weight ($W = G^+ - G^-$). To update G^+ and G^- each synapse was first determined whether in a potentiation or depression status based on the ΔW which was calculated via cross entropy loss and Adam optimizer,[73] as shown in Equation (1).

$$state = \begin{cases} potentiation, \ if \ \Delta W > 0 \\ depression, \ if \ \Delta W < 0 \end{cases} \quad (1)$$

For the weight updating in the potentiation state, G^+ is designed to an increase in conductance and G^- to a decrease and the reverse is applied during depressive updating, as shown in Equation (2).

$$\Delta G = G_{n+1} - G_n = \begin{cases} ae^{-\beta \frac{G_n - G_{min}}{G_{max} - G_{min}}}, \ if \ state = potentiation \\ -ae^{-\beta \frac{G_{max} - G_n}{G_{max} - G_{min}}}, \ if \ state = depression \end{cases} \quad (2)$$

Herein, G_n denotes the present conductance state of the synapse and G_{n+1} denotes the updated conductance state in the next training iteration, respectively. a denotes the step size of the conductance updating and β denotes the nonlinearity. Both G^+ and G^- are initialized to G_{min} when the synaptic conductance attains the maximum (G_{max}) or minimum (G_{min}) values to avoid over-scaling. All simulations were performed using Python, a free and open-source programming language, with SciPy and PyTorch packages. Codes are available from the corresponding author upon reasonable request.

Supporting Information

Supporting Information is available from the Wiley Online Library or from the author.

Acknowledgements

H.R. and A.G. thank Prof. Jianguo Mei and his research group for the fruitful discussion on the materials selection. This work was partially supported by the Abdul Latif Jameel Water and Food Systems (JWAFS) Lab at the Massachusetts Institute of Technology (S.Y., H.J.K.).

Conflict of Interest

The authors declare no conflict of interest.

Data Availability Statement

The data that support the findings of this study are available in the supplementary material of this article.

Keywords

artificial synapses, electrochromic polymers, electrolyte-gated transistors, ionic–electronic mixed conductors, neuromorphic computing

Received: May 3, 2023
Revised: June 20, 2023
Published online:

[1] D. D. Cox, T. Dean, *Curr. Biol.* **2014**, *24*, R921.
[2] S. B. Laughlin, R. R. de Ruyter van Steveninck, J. C. Anderson, *Nat. Neurosci.* **1998**, *1*, 36.
[3] V. Balasubramanian, *Proc. Natl. Acad. Sci. USA* **2021**, *118*, 2107022118.
[4] D. A. Drachman, *Neurology* **2005**, *64*, 2004.
[5] H. Markram, *Nat. Rev. Neurosci.* **2006**, *7*, 153.
[6] C. K. Machens, *Science* **2012**, *338*, 1156.
[7] D. Attwell, S. B. Laughlin, *J. Cereb. Blood Flow Metab.* **2001**, *21*, 1133.
[8] M. I. Posner, S. E. Petersen, *Annu. Rev. Neurosci.* **1990**, *13*, 25.
[9] Z. Wang, X. Wang, *IEEE Trans. Circuits Syst. I: Regul. Pap.* **2017**, *65*, 2210.
[10] D. Kireev, S. Liu, H. Jin, T. P. Xiao, C. H. Bennett, D. Akinwande, J. A. C. Incorvia, *Nat. Commun.* **2022**, *13*, 4386.
[11] F. Yu, L. Q. Zhu, H. Xiao, W. T. Gao, Y. B. Guo, *Adv. Funct. Mater.* **2018**, *28*, 1804025.
[12] M. Lanza, H. S. P. Wong, E. Pop, D. Ielmini, D. Strukov, B. C. Regan, L. Larcher, M. A. Villena, J. J. Yang, L. Goux, A. Belmonte, Y. Yang, F. M. Puglisi, J. Kang, B. Magyari-Köpe, E. Yalon, A. Kenyon, M. Buckwell, A. Mehonic, A. Shluger, H. Li, T. H. Hou, B. Hudec, D. Akinwande, R. Ge, S. Ambrogio, J. B. Roldan, E. Miranda, J. Suñe, K. L. Pey, et al., *Adv. Electron. Mater.* **2019**, *5*, 1800143.
[13] A. Gumyusenge, A. Melianas, S. T. Keene, A. Salleo, *Annu. Rev. Mater. Res.* **2021**, *51*, 47.
[14] S. B. Eryilmaz, D. Kuzum, R. Jeyasingh, S. B. Kim, M. BrightSky, C. Lam, H. S. Philip Wong, *Front. Neurosci.* **2014**, *8*, 205.
[15] A. A. Talin, Y. Li, D. A. Robinson, E. J. Fuller, S. Kumar, *Adv. Mater.* **2022**, 2204771.
[16] M. Huang, M. Schwacke, M. Onen, J. del Alamo, J. Li, B. Yildiz, *Adv. Mater.* **2022**, 2205169.
[17] H. Kang, J. Seo, H. Kim, H. W. Kim, E. R. Hong, N. Kim, D. Lee, J. Woo, *Micromachines* **2022**, *13*, 453.
[18] M. Onen, N. Emond, B. Wang, D. Zhang, F. M. Ross, J. Li, B. Yildiz, J. A. Del Alamo, *Science* **2022**, *377*, 539.
[19] M. Onen, N. Emond, J. Li, B. Yildiz, J. A. Del Alamo, *Nano Lett.* **2021**, *21*, 6111.
[20] X. Yao, K. Klyukin, W. Lu, M. Onen, S. Ryu, D. Kim, N. Emond, I. Waluyo, A. Hunt, J. A. del Alamo, J. Li, B. Yildiz, *Nat. Commun.* **2020**, *11*, 3134.
[21] E. J. Fuller, F. El Gabaly, F. Léonard, S. Agarwal, S. J. Plimpton, R. B. Jacobs-Gedrim, C. D. James, M. J. Marinella, A. A. Talin, *Adv. Mater.* **2017**, *29*, 1604310.
[22] Y. Li, T. P. Xiao, C. H. Bennett, E. Isele, A. Melianas, H. Tao, M. J. Marinella, A. Salleo, E. J. Fuller, A. A. Talin, *Front. Neurosci.* **2021**, *15*, 636127.
[23] Y. Van De Burgt, A. Melianas, S. T. Keene, G. Malliaras, A. Salleo, *Nat. Electron.* **2018**, *1*, 386.
[24] A. Melianas, T. J. Quill, G. LeCroy, Y. Tuchman, H. V. Loo, S. T. Keene, A. Giovannitti, H. R. Lee, I. P. Maria, I. McCulloch, A. Salleo, *Sci. Adv.* **2020**, *6*, eabb2958.
[25] Y. Lee, H. L. Park, Y. Kim, T. W. Lee, *Joule* **2021**, *5*, 794.
[26] Y. Van De Burgt, E. Lubberman, E. J. Fuller, S. T. Keene, G. C. Faria, S. Agarwal, M. J. Marinella, A. Alec Talin, A. Salleo, *Nat. Mater.* **2017**, *16*, 414.
[27] E. J. Fuller, S. T. Keene, A. Melianas, Z. Wang, S. Agarwal, Y. Li, Y. Tuchman, C. D. James, M. J. Marinella, J. J. Yang, A. Salleo, A. A. Talin, *Science* **2019**, *364*, 570.
[28] S. Jang, S. Jang, E. H. Lee, M. Kang, G. Wang, T. W. Kim, *ACS Appl. Mater. Interfaces* **2019**, *11*, 1071.
[29] X. Ji, B. D. Paulsen, G. K. K. Chik, R. Wu, Y. Yin, P. K. L. Chan, J. Rivnay, *Nat. Commun.* **2021**, *12*, 2480.
[30] Y. Fu, L. A. Kong, Y. Chen, J. Wang, C. Qian, Y. Yuan, J. Sun, Y. Gao, Q. Wan, *ACS Appl. Mater. Interfaces* **2018**, *10*, 26443.
[31] D. Lai, E. Li, Y. Yan, Y. Liu, J. Zhong, D. Lv, Y. Ke, H. Chen, T. Guo, *Org. Electron.* **2019**, *75*, 105409.
[32] J. Y. Gerasimov, R. Gabrielsson, R. Forchheimer, E. Stavrinidou, D. T. Simon, M. Berggren, S. Fabiano, *Adv. Sci.* **2019**, *6*, 1801339.
[33] S. Samal, H. Roh, C. E. Cunin, G. G. Yang, A. Gumyusenge, *Small* **2023**, 2207554.
[34] I. Krauhausen, D. A. Koutsouras, A. Melianas, S. T. Keene, K. Lieberth, H. Ledanseur, R. Sheelamanthula, A. Giovannitti, F. Torricelli, I. McCulloch, P. W. M. Blom, A. Salleo, Y. van de Burgt, P. Gkoupidenis, *Sci. Adv.* **2021**, *7*, eabl5068.
[35] P. M. Beaujuge, J. R. Reynolds, *Chem. Rev.* **2010**, *110*, 268.
[36] P. M. Beaujuge, S. Ellinger, J. R. Reynolds, *Nat. Mater.* **2008**, *7*, 795.
[37] P. Shi, C. M. Amb, E. P. Knott, E. J. Thompson, D. Y. Liu, J. Mei, A. L. Dyer, J. R. Reynolds, *Adv. Mater.* **2010**, *22*, 4949.
[38] B. Wang, J. Zhao, C. Cui, J. Liu, Q. He, *Sol. Energy Mater. Sol. Cells* **2012**, *98*, 161.
[39] H. W. Heuer, R. Wehrmann, S. Kirchmeyer, *Adv. Funct. Mater.* **2002**, *12*, 89.
[40] X. Li, K. Perera, J. He, A. Gumyusenge, J. Mei, *J. Mater. Chem. C* **2019**, *7*, 12761.
[41] S. T. M. Tan, A. Gumyusenge, T. J. Quill, G. S. LeCroy, G. E. Bonacchini, I. Denti, A. Salleo, *Adv. Mater.* **2022**, *34*, 211040.
[42] H. C. Ko, S. A. Park, W. K. Paik, H. Lee, *Synth. Met.* **2002**, *132*, 15.
[43] B. Lee, V. Seshadri, G. A. Sotzing, *Langmuir* **2005**,*21*, 10797.
[44] C. G. Wu, M. I. Lu, S. J. Chang, C. S. Wei, *Adv. Funct. Mater.* **2007**, *17*, 1063.
[45] A. L. Dyer, E. J. Thompson, J. R. Reynolds, *ACS Appl. Mater. Interfaces* **2011**, *3*, 1787.
[46] D. T. Christiansen, S. Ohtani, Y. Chujo, A. L. Tomlinson, J. R. Reynolds, *Chem. Mater.* **2019**, *31*, 6841.
[47] J. A. Kerszulis, C. M. Amb, A. L. Dyer, J. R. Reynolds, *Macromolecules* **2014**, *47*, 5462.
[48] D. T. Christiansen, J. R. Reynolds, *Macromolecules* **2018**, *51*, 9250.
[49] L. Nhon, R. Wilkins, J. R. Reynolds, A. Tomlinson, *J. Chem. Phys.* **2021**, *154*, 054110.

[50] A. Kumar, D. M. Welsh, M. C. Morvant, F. Piroux, K. A. Abboud, J. R. Reynolds, *Chem. Mater.* **1998**, *10*, 896.
[51] L. R. Savagian, A. M. Österholm, J. F. Ponder, K. J. Barth, J. Rivnay, J. R. Reynolds, *Adv. Mater.* **2018**, *30*, 1804647.
[52] B. D. Reeves, C. R. G. Grenier, A. A. Argun, A. Cirpan, T. D. McCarley, J. R. Reynolds, *Macromolecules* **2004**, *37*, 7559.
[53] U. Salzner, *J. Phys. Chem. B* **2002**, *106*, 9214.
[54] C. M. Amb, P. M. Beaujuge, J. R. Reynolds, *Adv. Mater.* **2010**, *22*, 724.
[55] D. M. WelshSkotheim, A. Kumar, E. W. MeijerElsenbaumer, J. R. Reynolds, *IAdv. Mater.* **1999**, *11*, 1379.
[56] J. Roncali, *Chem. Rev.* **1997**, *97*, 173.
[57] J. Roncali, *Macromol. Rapid Commun.* **2007**, *28*, 1761.
[58] A. Giovannitti, K. J. Thorley, C. B. Nielsen, J. Li, M. J. Donahue, G. G. Malliaras, J. Rivnay, I. McCulloch, *Adv. Funct. Mater.* **2018**, *28*, 1706325.
[59] J. He, L. You, J. Mei, *ACS Appl. Mater. Interfaces* **2017**, *9*, 34122.
[60] C. Angeli, B. Bories, A. Cavallini, R. Cimiraglia, *J. Chem. Phys.* **2006**, *124*, 054108.
[61] F. Neese, *Wiley Interdiscip. Rev.: Comput. Mol. Sci.* **2012**, *2*, 73.
[62] A. D. Becke, *J. Chem. Phys.* **1993**, *98*, 5648.
[63] E. Caldeweyher, S. Ehlert, A. Hansen, H. Neugebauer, S. Spicher, C. Bannwarth, S. Grimme, *J. Chem. Phys.* **2019**, *150*, 154122.
[64] A. D. Becke, E. R. Johnson, *J. Chem. Phys.* **2005**, *123*, 154101.
[65] F. Weigend, R. Ahlrichs, *Phys. Chem. Chem. Phys.* **2005**, *7*, 3297.
[66] V. Barone, M. Cossi, *J. Phys. Chem. A* **1998**, *102*, 1995.
[67] C. Cendra, A. Giovannitti, A. Savva, V. Venkatraman, I. McCulloch, A. Salleo, S. Inal, J. Rivnay, *Adv. Funct. Mater.* **2019**, *29*, 1807034.
[68] S. T. M. Tan, S. Keene, A. Giovannitti, A. Melianas, M. Moser, I. McCulloch, A. Salleo, *J. Mater. Chem. C* **2021**, *9*, 12148.
[69] F. Torricelli, D. Z. Adrahtas, Z. Bao, M. Berggren, F. Biscarini, A. Bonfiglio, C. A. Bortolotti, C. D. Frisbie, E. Macchia, G. G. Malliaras, I. McCulloch, M. Moser, T. Q. Nguyen, R. M. Owens, A. Salleo, A. Spanu, L. Torsi, *Nat. Rev. Methods Primers* **2021**, *1*, 66.
[70] H. Roh, C. Cunin, S. Samal, A. Gumyusenge, *MRS Commun.* **2022**, *12*, 565.
[71] A. Giovannitti, D. T. Sbircea, S. Inal, C. B. Nielsen, E. Bandiello, D. A. Hanifi, M. Sessolo, G. G. Malliaras, I. McCulloch, J. Rivnay, *Proc. Natl. Acad. Sci. USA* **2016**, *113*, 12017.
[72] Y. LeCun, L. Bottou, Y. Bengio, P. Haffner, *Proc. IEEE* **1998**, *86*, 2278.
[73] S. Kim, B. Choi, M. Lim, J. Yoon, J. Lee, H. D. Kim, S. J. Choi, *ACS Nano* **2017**, *11*, 2814.
[74] J. Sun, S. Oh, Y. Choi, S. Seo, M. J. Oh, M. Lee, W. B. Lee, P. J. Yoo, J. H. Cho, J. H. Park, *Adv. Funct. Mater.* **2018**, *28*, 1804397.
[75] S. Seo, J. J. Lee, R. G. Lee, T. H. Kim, S. Park, S. Jung, H. K. Lee, M. Andreev, K. B. Lee, K. S. Jung, S. Oh, H. J. Lee, K. S. Kim, G. Y. Yeom, Y. H. Kim, J. H. Park, *Adv. Mater.* **2021**, *33*, 2102980.
[76] Y. Zhao, C. Su, G. Shen, Z. Xie, W. Xiao, Y. Fu, S. Inal, Q. Wang, Y. Wang, W. Yue, I. McCulloch, D. He, *Adv. Funct. Mater.* **2022**, *32*, 2205744.
[77] A. Melianas, M.-A. Kang, A. VahidMohammadi, T. J. Quill, W. Tian, Y. Gogotsi, A. Salleo, M. M. Hamedi, *Adv. Funct. Mater.* **2022**, *32*, 2109970.